AGU PUBLICATIONS

JGR

Journal of Geophysical Research: Solid Earth

RESEARCH ARTICLE
10.1002/2014JB011666

Key Points:
- New large-scale experimental facility synthesizes life-scalable PDCs
- Experimental currents analogous to pyroclastic flows and surges can be produced
- Experimental deposits have characteristics of natural pendants

Correspondence to:
G. Lube,
g.lube@massey.ac.nz

Citation:
Lube, G., E. C. P. Breard, S. J. Cronin, and J. Jones (2015), Synthesizing large-scale pyroclastic flows: Experimental design, scaling, and first results from PELE, *J. Geophys. Res. Solid Earth*, *120*, doi:10.1002/2014JB011666.

Received 6 OCT 2014
Accepted 20 JAN 2015
Accepted article online 23 JAN 2015

Synthesizing large-scale pyroclastic flows: Experimental design, scaling, and first results from PELE

G. Lube[1], E. C. P. Breard[1], S. J. Cronin[1], and J. Jones[2]

[1]Volcanic Risk Solutions, Massey University, Palmerston North, New Zealand, [2]School of Engineering and Advanced Technology, Massey University, Palmerston North, New Zealand

Abstract Pyroclastic flow eruption large-scale experiment (PELE) is a large-scale facility for experimental studies of pyroclastic density currents (PDCs). It is used to generate high-energy currents involving 500–6500 m^3 natural volcanic material and air that achieve velocities of 7–30 m s^{-1}, flow thicknesses of 2–4.5 m, and runouts of >35 m. The experimental PDCs are synthesized by a controlled "eruption column collapse" of ash-lapilli suspensions onto an instrumented channel. The first set of experiments are documented here and used to elucidate the main flow regimes that influence PDC dynamic structure. Four phases are identified: (1) mixture acceleration during eruption column collapse, (2) column-slope impact, (3) PDC generation, and (4) ash cloud diffusion. The currents produced are fully turbulent flows and scale well to natural PDCs including small to large scales of turbulent transport. PELE is capable of generating short, pulsed, and sustained currents over periods of several tens of seconds, and dilute surge-like PDCs through to highly concentrated pyroclastic flow-like currents. The surge-like variants develop a basal <0.05 m thick regime of saltating/rolling particles and shifting sand waves, capped by a 2.5–4.5 m thick, turbulent suspension that grades upward to lower particle concentrations. Resulting deposits include stratified dunes, wavy and planar laminated beds, and thin ash cloud fall layers. Concentrated currents segregate into a dense basal underflow of <0.6 m thickness that remains aerated. This is capped by an upper ash cloud surge (1.5–3 m thick) with 10^0 to 10^{-4} vol % particles. Their deposits include stratified, massive, normally and reversely graded beds, lobate fronts, and laterally extensive veneer facies beyond channel margins.

1. Introduction

Pyroclastic density currents (PDCs; pyroclastic flows and surges) are the most deadly volcanic thread known to humankind. They are swiftly flowing, hot, and mostly ground-hugging mixtures of volcanic particles and gas that form during the gravitational collapse of eruption columns, pyroclastic fountains, and lava domes [*Freundt et al.*, 2000; *Sulpizio et al.*, 2014]. Particularly violent PDCs emerge from rapid lateral expansion of gas-particle mixtures during sudden decompression of domes, cryptodomes, conduits, and hydrothermal systems [*Freundt and Bursik*, 1998; *Wohletz*, 1998]. In all these cases extreme fatalities, property destruction, and landscape erosion arise as a combination of PDC velocities, destructive forces, and heat, along with their interaction with rough and tortuous surfaces and acceleration at rapid changes in slope or topographic barriers [e.g., *Taylor*, 1958; *Hoblitt et al.*, 1981; *Waitt*, 1981; *Valentine*, 1998; *Calder et al.*, 1999; *Cronin et al.*, 2013; *Jenkins et al.*, 2013].

To improve our physical understanding of PDCs, researchers have relied upon direct syneruption observations, field studies on deposits, analogue experiments, and computational modeling. The extreme violence of PDCs makes safe observations difficult, and data remain limited to broad estimates of bulk flow behavior of the outer cloud [e.g., *Levine and Kieffer*, 1991; *Lube et al.*, 2011]. Thus, most of our current knowledge of PDCs stems from interpretations of the geometric, sedimentary, and also geochemical features of their deposits. This leaves major fundamental gaps open in our understanding of the gas-particle transport and sedimentation processes of PDCs. In turn, translating field results into testable physical models of PDC dynamics remains a particular challenge. Under such circumstances, analogue experiments provide a key insight, although technical and scale limitations reduce these to simplified end-members. However, the few laboratory experiments that have started to explore simplified end-member flow regimes that are inferred to exist in PDCs did not scale to their natural pendants [*Burgisser et al.*, 2005]. Numerical models can provide alternative insights, but improved constitutive relationships and validation and calibration data sets are needed to truly evaluate their effectiveness.

Despite decades of study, major gaps remain in understanding PDCs that include a detailed knowledge of the physical processes behind their runout and destruction behavior. Missing in particular is a characterization of the scales of turbulence and the modes of dynamic feedback between hot particles and gas. This is needed to develop fundamental theories for dynamic portioning of energy, mass, and forces in hot, compressible gas-particle mixtures. Further, quantitative sediment transport and deposition models (underlying these theories and linking PDC flow dynamics with deposit characteristics) are still in their infancies (e.g., *Dellino et al*. [2008] for dilute PDCs) and are also largely debated.

Naturally optimal international testing sites have been used to understand some Earth surface geophysical mass flows (e.g., the Norwegian Snow avalanche Research Centre in Ryggfonn and the Chinese Debris Flow Observation and Research Station in Dongchuan). But the lack of regular, safe viewing possibilities has led to the international community identifying an urgent priority for large-scale experimental approaches to understanding PDC hazards [*Valentine et al*., 2011]. After 4 years of construction and testing efforts, here we report on an experimental apparatus christened "PELE" (pyroclastic flow eruption large-scale experiment), which has been used for a first systematic series of large-scale PDC experiments that achieve full scaling similitude to natural PDCs. PELE is a permanent international research facility, currently located at Massey University in New Zealand.

A main objective for the design of PELE was to repeatedly synthesize high-energy gas-particle mixture flows that cover the widest possible range of natural PDC transport and deposition regimes. Volcanic material with their natural grain size, density, and particle shape characteristics is used as the solid phase and air as the fluid phase. This is an important prerequisite to ensure natural stress coupling between solid and fluid phases and to allow for quantitative comparisons between experimental and real-world deposits [e.g., *Dellino et al*., 2007]. However, these conditions force strict lower limits on the minimum length scale, velocity, and duration of the targeted experimental flows that are far greater than those reached in analogue experiments benchtop scale.

PELE was designed as extension from other novel large-scale pyroclastic surge analogue experiments produced by vertical explosion and axisymmetric spreading [*Dellino et al*., 2007]. Omitting vertical explosions, PELE is used to generate higher-volume and high particle concentration high-energy gas-particle flows in a channel setting. Up to 4.2 m^3 of pyroclastic material is used in each experimental run. This paper documents the fundamental experimental design of the new facility and explains how sustained and pulsed currents with controllable properties and a wide range of particle concentration ($<<$1 to 55 vol %) are generated and observed. We use the first suite of experiments to provide new insights into the range of experimental PDC transport regimes and their relationships to deposit types. In addition, we document dynamic and kinematic scaling of the PELE flows to concentrated and dilute PDCs (i.e., pyroclastic flows and surges).

2. PELE—The Pyroclastic Flow Generator

2.1. Design and Engineering

Similar to the collapse of eruption columns to the slopes of a volcano, PELE synthesizes experimental pyroclastic density currents by the controlled gravitational collapse of variably diluted suspensions of pyroclasts and gas into an inclinable channel. This process was adopted from nature as an effective mechanism to create a wide range of replicable flow conditions through systematic changes of the starting and boundary condition of collapses.

PELE is operated indoors, inside a 16 m high, 25 m long, and 18 m wide disused boiler house. This installation contains four main structural components (Figure 1a):

1. Tower. A 13 m high structure that supports two types of hoppers through which column collapses can be initiated. These are moved in an elevator-like system to user-specified discharge heights. There is a semiautomated hopper filling rig, a hopper aeration unit, and a hopper heating system.
2. Column. An up to 9 m high shroud through which air particle mixtures fall beneath the suspended hopper.
3. Chute. A 12 m long channel section, variably adjustable between 5 and 25° slope angles and with sides up to 0.6 m high.
4. Outflow. A 25 m long flat, smooth runout section that extends outside the building.

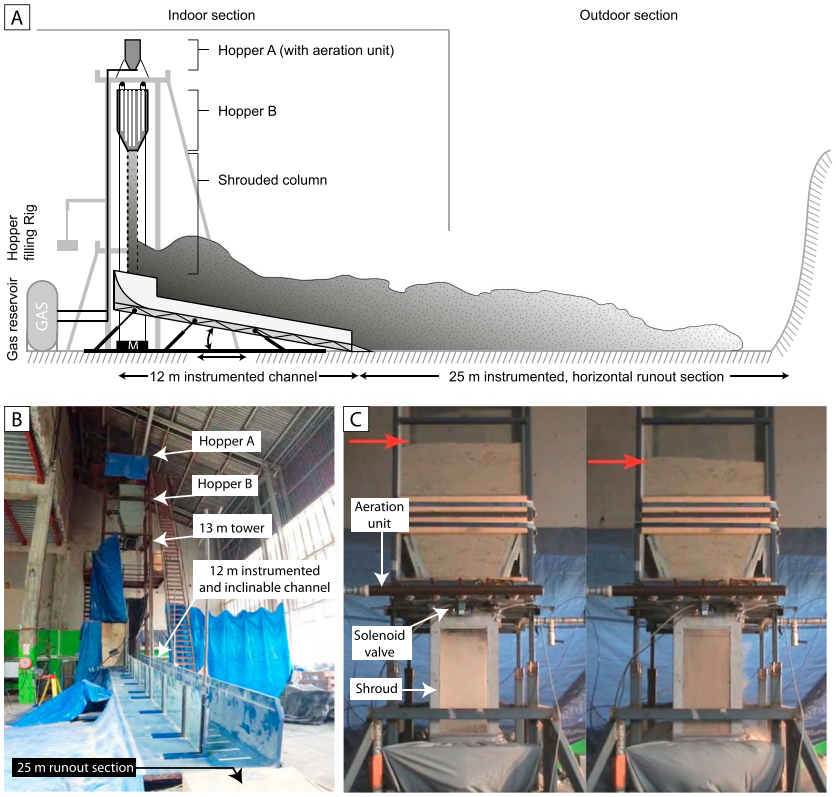

Figure 1. Components of the pyroclastic flow generator. (a) Setup sketch of PELE depicting the PDC tower (including hoppers A and B, hopper elevator, filling and heating platform, and aeration unit); the free-fall section; the inclined wall-bounded channel; and the horizontal runout section. (b) Overview photograph of the indoor part of the setup. (c) Close-up of aeratable hopper A at 2 times during discharge. Red arrows indicate upper level of solids material.

PELE was designed to allow for the independent adjustment of several initial PDC flow conditions, including the physical characteristics of the gas-particle suspensions at the instance of impact with the flow channel (Table 1). The impact velocity U_I of the particle-air collapses can be varied between 4.7 and 11 m s^{-1}, with an impact volume flux Q_{V_I} of 2.8 to 6.5 m^3 s^{-1}, equating to a mass flux Q_{M_I} of 32 to 1037 kg s^{-1}. The initial particle solids concentration of the collapsing suspension C_I is varied between 0.5 and 18.5 vol % leading to collapse durations T_C between <1 and 21 s. The grain size distribution and density of the solid phase (see section 2.4) and its temperature are also controlled (room temperature to 300°C). For experiments above room temperature a 7.5 kW heating system consisting of nine heating elements is inserted inside the hopper heating the particles before the experimental run.

Table 1. Initial and Boundary Conditions of Experiments and Ranges of Flow Parameters During Column Collapse Impact

Parameter	Symbol	Minimum	Maximum
Hopper and Boundary Condition Parameters			
Initial solids mass	M_I	<100 kg	4150
Hopper mass discharge	Q_{MH}	31 kg s^{-1}	1591 kg s^{-1}
Drop height	h_D	1.2 m	11 m
Channel inclination	β	5°	25°
Channel width	W_C	0.35 m	1.5 m
Temperature	T_H	15°C	300°C
Column Collapse Impact Parameters			
Impact velocity	U_I	4.7 m s^{-1}	11 m s^{-1}
Impact mass flux	Q_{MI}	32 kg s^{-1}	1591 kg s^{-1}
Impact volume flux	Q_{VI}	2.8 m^3 s^{-1}	6.5 m^3 s^{-1}
Impact particle concentration	ρ_I	0.5 vol %	18.5 vol %

The main (variable) boundary conditions of the PELE experiments are the channel width W_C (0.35 to 1.5 m), the channel inclination β (5 to 25°), and the channel floor roughness L_R (varied through inserts). In future, other terrain elements including curved or laterally confining/widening channel sections and vertical cliffs can be added readily.

Through repeating experimental runs, we started to explore the degree of reproducibility of experiments conducted at these large scales. For two experiments with the same starting and boundary conditions, the variability of the deposit geometry can be assessed as the differences in deposit height at the same runout location and as the difference in deposit length. These differences account to less than 5%. The overall large-scale eddy structure in repeated runs is fairly reproducible with the total number of the largest-sized eddies (typically >1 m), their individual total heights and their average rotational velocities at similar runout lengths varying by less than 10%. Any smaller-scale eddy structures differ from one run to another and cannot be reproduced. We noticed that the largest source of error in our experiments arises from the spatial heterogeneity of the material filled into the hopper. Hence, a semiautomated filling method is used to reduce the spatial variation in grain size distribution and material compaction. Through this method, variation in discharge rate is kept between 5 and 10%.

2.2. Synthesizing Eruption Column Collapses

To cover a wide range of initial kinematic properties, two custom-made hoppers with maximum fill levels of 0.75 m^3 (hopper A; Figure 1c) and 4.2 m^3 (hopper B; Figures 1a and 1b) and different adjustable ranges in discharge rate are used. Both hoppers are suspended on four load cells to monitor the time-dependent discharge. Experiments are triggered via remotely controlled, high-speed trapdoors at the base of each hopper. Hopper A can be operated in mass flow regime (the engineering term for discharge at constant mass flow rate) for discharge rates Q_{MH} between 31 and 123 kg s^{-1} of low-density Taupo ignimbrite mixtures (see section 2.4 below), while hopper B yields constant mass flow rates in the range from 204 to 1591 kg s^{-1}. Higher discharge rates are obtained with denser particulates.

In hopper A, used to generate experimental PDCs with low to intermediate particle concentrations, the discharge rate is regulated via an aeration system, with air bars that cross the base of the outlet. Up to 0.56 m^3 s^{-1} of gas are injected from five air bars as horizontal sheets into the falling particles. Each air bar contains 256 pairs of opposing 1 mm diameter micronozzles to homogeneously aerate the mixture. Gas supply to the air bars is fed from two header sections that are connected to a large, high-pressure reservoir. The gas lines are pressurized before the experiment to target pressure within inline regulators and opened by solenoid valves 100 ms before trapdoor release. The flow rate of gas that can be delivered through the air bars is restricted by the maximum possible area of the nozzles, which must be less than twice the cross-sectional area of each air bar. This ensures that choking can only occur at the nozzles. Figure 2a depicts the linear relationship between solid mass flow rate and gas flow rate from the air bars for experiments with Taupo ignimbrite material.

In hopper B, synthesizing experimental PDCs with intermediate to high solids concentrations, discharge is controlled by two mechanisms. A set of three vertically tapering wedge sections can be mounted to the hopper base to vary the maximum outlet area. In addition, two types of metal screens for each wedge section can be inserted above the hopper outlet to further constrain the effective hopper outflow area resulting in a total of nine different discharge settings.

Figure 2b illustrates the variability in discharge behavior for two experiments with low hopper flow rates using hopper A (experiment S10_8.5 with total mass $M_I = 85.7$ kg; $Q_{MH} = 32$ kg s^{-1}) and high flow rates with hopper B (experiment PF10_5 with $M_I = 1249$ kg; $Q_{MH} = 886$ kg s^{-1}). In these cases constant mass flow rates occur for approximately 80% (hopper A) and close to 100% (hopper B) of the total discharge time.

The opening of the hopper initiates an "eruption column collapse" as a descending stream of particles that forms a central, dense, and downward dilating core region of relatively constant cross-sectional area, surrounded by a translucent turbulent boundary layer of entrained air that expands downward. The downward tapering shroud below the hopper opening reduces air entrainment and ensures the falling suspension has a known solids concentration and is directed precisely into the channel. It also ensures that the impact area, A_i, equals the hopper outlet area. The mass of particles entrained into the outer turbulent boundary layer shell could be directly sampled in some experiments and is always $<<1$% of the total mass discharged. Hence, the amount of air mass entrained during vertical acceleration is negligible, and the density of the

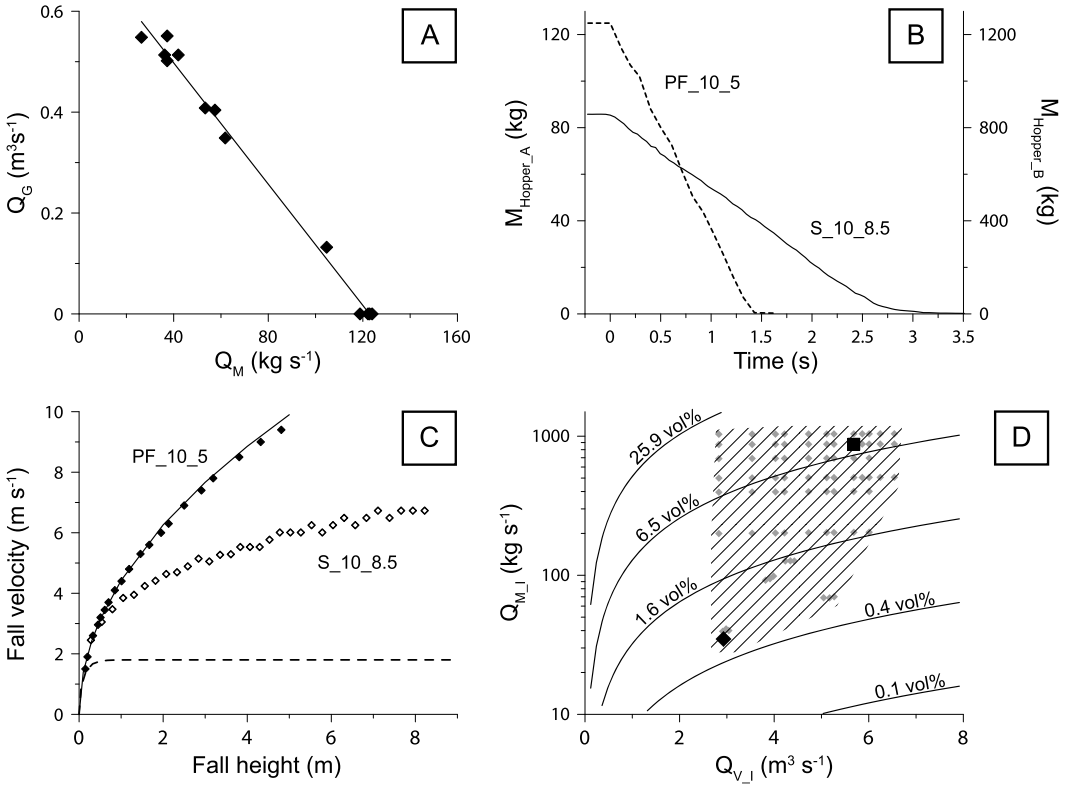

Figure 2. Characteristics of material discharge and dilution during eruption column collapse. (a) Data of solids flow rate and gas flow rate for hopper A using the aeration unit. The solid line depicted is a best fit linear regression to the data. (b) Hopper mass against time plot for experiments S_10_8.5 using hopper A and PF_10_5 using hopper B. (c) Velocity of the leading front of the freely falling suspension against time for S_10_8.5 and PF_10_5. The solid line shows the theoretical free-fall law in vacuum. The dashed line depicts the theoretical free-fall law including drag for a single particle with a median diameter corresponding to the coarsest clast of the experimental mixture. (d) Phase diagram of the range of initial kinematic conditions of PDCs at the instance of impact showing data of initial volume flux Q_{V_I}, initial mass flux Q_{M_I}, and lines of equal particle solids concentration C_I. Initial impact conditions for PDCs S_10_8.5 (black diamond) and PF_10_5 (black square) are also shown.

suspension at the instance of impact ρ_i can be approximated through the recorded data of hopper mass flow rate, Q_{MH}, impact area, A_i, and impact velocity, U_i as

$$\rho_i = \frac{Q_{MH}}{A_i U_i} \tag{1}$$

Figure 2c depicts the velocity of the leading front of the collapsing suspension against distance for experiments S10_8.5 and PF10_5 with drop heights h_D of 8.5 m and 5 m, respectively. Initially, the velocities of the two suspensions closely follow the free-fall law in vacuum conditions. In the low mass flux run, S10_8.5, drag becomes apparent after roughly 0.5 s and the impact density ρ_i amounts to 12 ± 0.2 kg m^{-3} (approximately 0.6 vol %). In the high mass flux run, PF10_5, the impact velocity is approximately 3% lower than that predicted by nondrag free fall and ρ_i is 154 ± 11 kg m^{-3} (approximately 7.8 vol %). In a vertically accelerating stream of homogeneous liquid, a constant density is maintained through the reduction in cross-sectional area. In our case, where the cross-sectional area is (kept) constant and air entrainment is very low, bulk density decreases through the development of an under pressure in the mixture. Due to the curvature of the impact area inside the channel, the drop height (and corresponding dilution) increases slightly in downstream direction and lies within the range in mixture density around the average values reported above.

The construction dimensions of PELE define minima and maxima in drop height and discharge rate and the possible parameter space for the volume flux Q_{V_I} (varying by a factor of 2.3) and mass flux Q_{M_I} (varying by a factor of 30) of the impacting suspension onto the channel (Figure 2d). This yields initial suspension concentrations between ≤ 1 and 30 vol % particles.

2.3. Measuring Into Experimental PDCs

Three high-speed cameras (operated between 340 and 3000 frames per second (fps)), two fast cameras (60 to 120 fps), and two normal-speed cameras (24 to 30 fps) positioned at different distances, viewing angles and directions, record the downstream evolution of the experimental PDCs. The high-temperature glass walls of the channel are illuminated by a 5500 W light array and allow for a detailed analysis of the gas-particle transport and sedimentation processes with particle image velocimetry (PIV; using the algorithm PIVlab [*Thielicke and Stamhuis*, 2014]). Four pressure transducers and two load cells are mounted into the channel floor at different distances to measure the basal gas pore pressure and mass of the passing current. Variations of gas pressure with flow height are recorded perpendicular to flow and at 5 cm in from the channel walls using 2.5 mm diameter needle-shaped probes that protrude through the lateral flow boundary layer. A total of 64 sediment catchers are installed in four vertical arrays along the flow path to obtain the time-averaged mass flux as well as time-averaged grain size distributions of the PDCs at variable heights. In the most recent experiments, 40 reflective (near)-infrared sensors (850 nm wavelength) are used to measure time-variant mixture density. This method is based on a strong, nonlinear correlation between mixture density (in the range from approximately 1.3 kg m^{-3} to approximately 200 kg m^{-3}) and (material-specific) reflectance measured by the sensors. Synchronized spot measurements of time-variant (near)-infrared sensor reflectance and time-variant mixture density (direct measurement) were used to quantify the empirical relationship in test experiments. For the direct measurements of mixture density, we recorded with high-speed video the sequential filling of transparent, horizontally oriented glass tubes with cross-sectional area, A_p, that were installed next to each near-infrared sensor. The tubes were open on the upstream side to collect the flow over the tube cross-sectional area and contained an 8 μm mesh at their downstream side impermeable for particles and permeable for air. Mixture density is obtained as $\rho_F(t) = Q_{VF}(t)\rho_S/A_lU_i(t)$, where Q_{VF} is the volumetric rate of sediment accumulation in the tube, ρ_S is the uncompacted bulk material density, U_i is the velocity of the flow before entering the tube (measured by PIV), and t is time. In flow experiments, the calibrated IR sensors are installed in three vertical arrays at variable distances in the channel to image any vertical density stratification. Three National Instruments data loggers record the sensor signals at a rate of up to 5 kHz together with a synchronization trigger pulse that opens the hopper and illuminates high-speed light-emitting diodes in the view of the cameras.

2.4. Material

After a number of test experiments with polystyrene beads and beach sands, the main series of PDC experiments were conducted with natural pyroclastic material from the AD233 Taupo eruption (*Wilson* [1985] for deposit details). Systematic variations of the material grain size distribution are achieved by blending two separate depositional units of the Taupo ignimbrite (Figures 3a and 3b). The first component (F1) is a proximal medium-ash-dominated ignimbrite deposit with a unimodal grain size distribution, a median diameter of 366 μm, and 4.5 wt % of extremely fine ash (<63 μm). The second component (F2) is fine ash-rich facies from the base of the proximal Taupo ignimbrite, showing a polymodal distribution, median diameter of 103 μm, and 36.5 wt % extremely fine ash. Large volumes of both PDC deposits were mined in the field, dried, and stored in air-tight 55 L containers for their later use in the experiments. The blending of both components at mass fractions of component F2 from 0 to 40% yields natural PDC grain size characteristics with unimodal, poorly to very poorly sorted distributions (with a sorting coefficient σ_ϕ: 2.128 to 1.692 phi), particle sizes from 22 mm to 1.4 μm, with median diameters Md_ϕ between 241 and 366 μm, and <63 μm fractions between 4.5 and 17 wt % (Figures 3c and 3d). Components include highly vesicular pumice, loose crystals, dense juvenile particles, and dense lithics. The bulk solid density of the material varies strongly with grain size from approximately 400 kg m^{-3} for sizes coarser than −8 mm and approximately 2600 kg m^{-3} for sizes finer than 63 μm (Figure 3e). With an increase of component F2 from 0 to 40%, the uncompacted bulk material density of the mixture is increasing from 840 to 990 kg m^{-3}.

3. Synthesizing Pyroclastic Density Currents

3.1. Flow Phases and General Characteristics

The routine preparations for each experiment with PELE include setting channel inclination, width and floor roughness, the fine calibration of sensors, setup of cameras and lighting, hopper filling, setting hopper discharge height, mounting of shrouding and aeration units, connection of the pneumatic trapdoor release

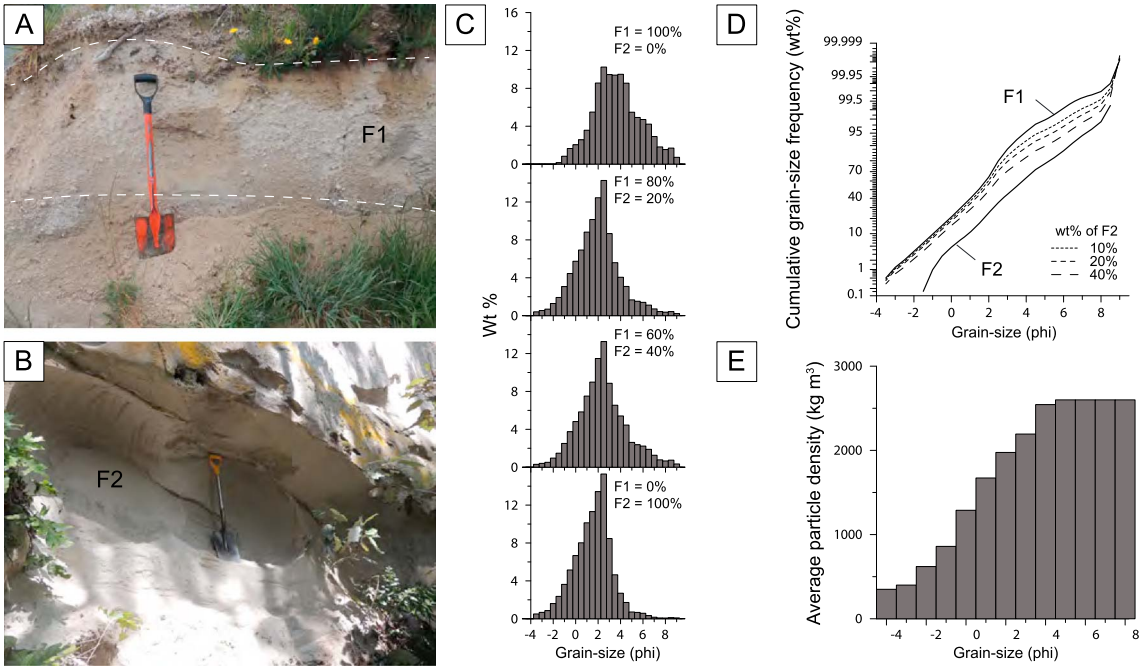

Figure 3. Material characteristics. (a and b) Outcrop photographs of mixture components F1 (medium-ash-dominated facies of ignimbrite) and F2 (fines-rich base of ignimbrite) of the AD233 Taupo eruption. (c) Grain size distributions of experimental mixtures in histogram form at variable weight fractions of component F2. (d) Grain size distributions of experimental mixtures in cumulative form at variable weight fractions of component F2. (e) Average clast density against particle size in phi units for the experimental material.

system, and heating of the experimental material. From remote triggering, over PDC runout, until complete settling of the ash cloud each experiment lasted an hour or two. The geometry of the deposit is recorded through scans with a Leica Terrestrial Laser Scanner before and after an experiment. The deposit thickness, mass per unit area, and grain size distribution are measured in profiles longitudinally and perpendicularly to flow (especially where laterally expanding ash cloud surges are deposited). Four phases can be distinguished during each experimental run:

1. Phase (1): *Eruption column collapse*. After discharge of the concentrated gas-particle mixture it accelerates and dilutes during free fall onto the inclined channel. This phase lasts between $<$1.5 and up to ~21 s, depending on the hopper discharge rate and material volume. These settings produce short and pulsed collapses through to sustained current feeding.
2. Phase (2): *Impact and lateral mixture expansion*. The collapsing particle suspension is guided into an inclined channel along a 2 m long and 1.2 m high curved slope. During impact, the majority of the material accelerates longitudinally along the channel. This is accompanied by air entrainment and mixture expansion leading to dilution. The mixture, traveling at 7 to 30 m/s expands longitudinally and advects vigorously, becoming fully turbulent within the first 1.5 m of impact (see scaling section below). A minor fraction of the collapsing mass radiates outward from the impact zone forming an advecting, 4–8 m high plume, 2–4 m downstream of the impact area.
3. Phase (3): *Pyroclastic density current phase*. The pyroclastic density current phase is demonstrated by a strongly stratified shear flow propagating along 12 m of inclined section, followed by an unconstrained runout onto a distal horizontal surface. The 0.6 m high channel walls contain the bulk flowing mass. Despite this, strong advection generates large dilute clouds of ash and gas that billow outward and upward. Deposition of channel-confined flow material and lateral clouds of ash starts within approximately 3.5–30 s of experiment onset.
4. Phase (4): *Escaping ash cloud expansion and deposition*. Following deposition of most of the mass, ~5% of particles remain in suspension to form an approximately 2000–5000 m^3 cloud of fine and very fine ash. The complete settling of particles from this takes 1–2 h depending on the grain size distribution of the initial mixture.

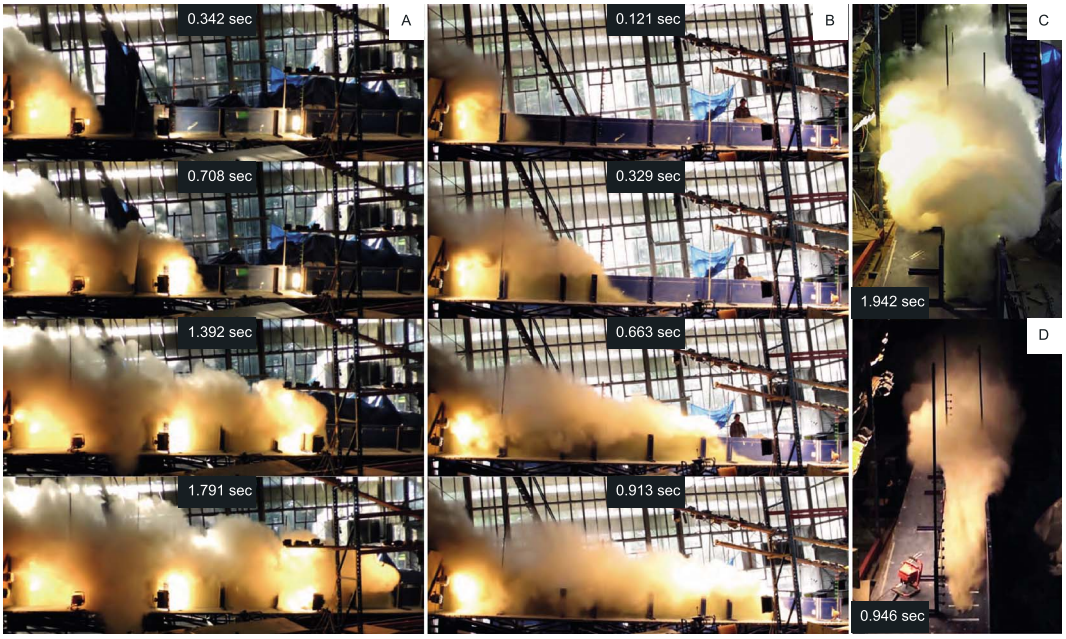

Figure 4. Photographs of (a and c) dilute PDC run S_10_8.5 and (b and d) concentrated PDC run PF_10_5 at times when the flow front has reached similar runout distance from the impact zone. See section 3.2 for detailed flow descriptions.

3.2. End-Member Flow Regimes—Simulating Pyroclastic Surges Versus Pyroclastic Flows

Experiments S_10_8.5 and PF_10_5 (Figure 4) document two contrasting current behaviors at room temperature that were simulated at PELE, by varying drop height (5 and 8.5 m, respectively), solid mass (85.8 kg and 1249 kg), and hopper discharge rate (32 and 886 kg s^{-1}). The initial grain size distribution for the two experiments was identical using a mixture with 20 wt % of component F2 (see Figure 3c). This blend had a median particle diameter of 0.33 mm, a sorting coefficient of 1.78 phi and 11 wt % particles <63 μm, while the internal and basal friction angles were 39° and 36.5°, respectively. The channel slope and widths were set at 10° and 0.5 m, respectively, with a rough, nonerodible base of stainless steel.

3.2.1. Phase (1)

Impact of the falling suspensions with the channel occurs 1.74 s (S_10_8.5) and 1.01 s (PF_10_5) after hopper discharge triggering. The S_10_8.5 flow reached a vertical impact velocity U_I of 6.89 m s^{-1}, intermediate between the theoretical free-fall velocity in vacuum and terminal velocity (including drag) of the maximum clast diameter of the natural particle mixture (Figure 5a). The PF_10_5 column collapse attained a velocity $U_I = 9.48$ m s^{-1}, slightly slower than the corresponding vacuum free-fall value (Figure 5b). The impact mass flux Q_{M_I} (34.62 kg s^{-1} and 874.64 kg s^{-1}, respectively) and impact volume flux Q_{V_I} (2.93 m^3 s^{-1} and 5.69 m^3 s^{-1}, respectively) show strongly contrasting initial dilution, equivalent to particle concentrations of 0.6 vol % for S_10_8.5 and 7.8 vol % for PF_10_5 (Figure 2d).

3.2.2. Phase (2)

Immediately downstream of the 1.2 m long impact zone, flow front and flow internal velocities are substantially larger than the impact velocity. For S_10_8.5 at 1.9 m downslope, they are 8.5 m s^{-1} at the flow front and 9 m s^{-1} as a maximum internal velocity. This is 20–30% higher than the impact velocity. In PF_10_5, at 2 m the mixture attained frontal velocities of 24 m s^{-1} and maximum internal velocities of 29 m s^{-1}, values of up to 250% of U_I. Assuming mass conservation, the corresponding dilution within Phase (2) at certain runout distances was calculated by comparing the impact volume flux Q_{V_I} with the local volume flux Q_{V_P} (computed as the ratio of the differential of digitized flow volume in neighboring frames of the footage and time difference between the frames) as

$$C_P = \frac{C_{V_I} Q_{V_I}}{Q_{P_I}}, \tag{2}$$

where C_P is particle volume concentration. For S_10_8.5 at 2 m, C_P accounts to approximately 0.2 vol %. For PF_10_5 at 2.5 m, the mixture has diluted to an average concentration $C_P = 3$ vol %. At this stage and $<1 \times 10^{-2}$ s

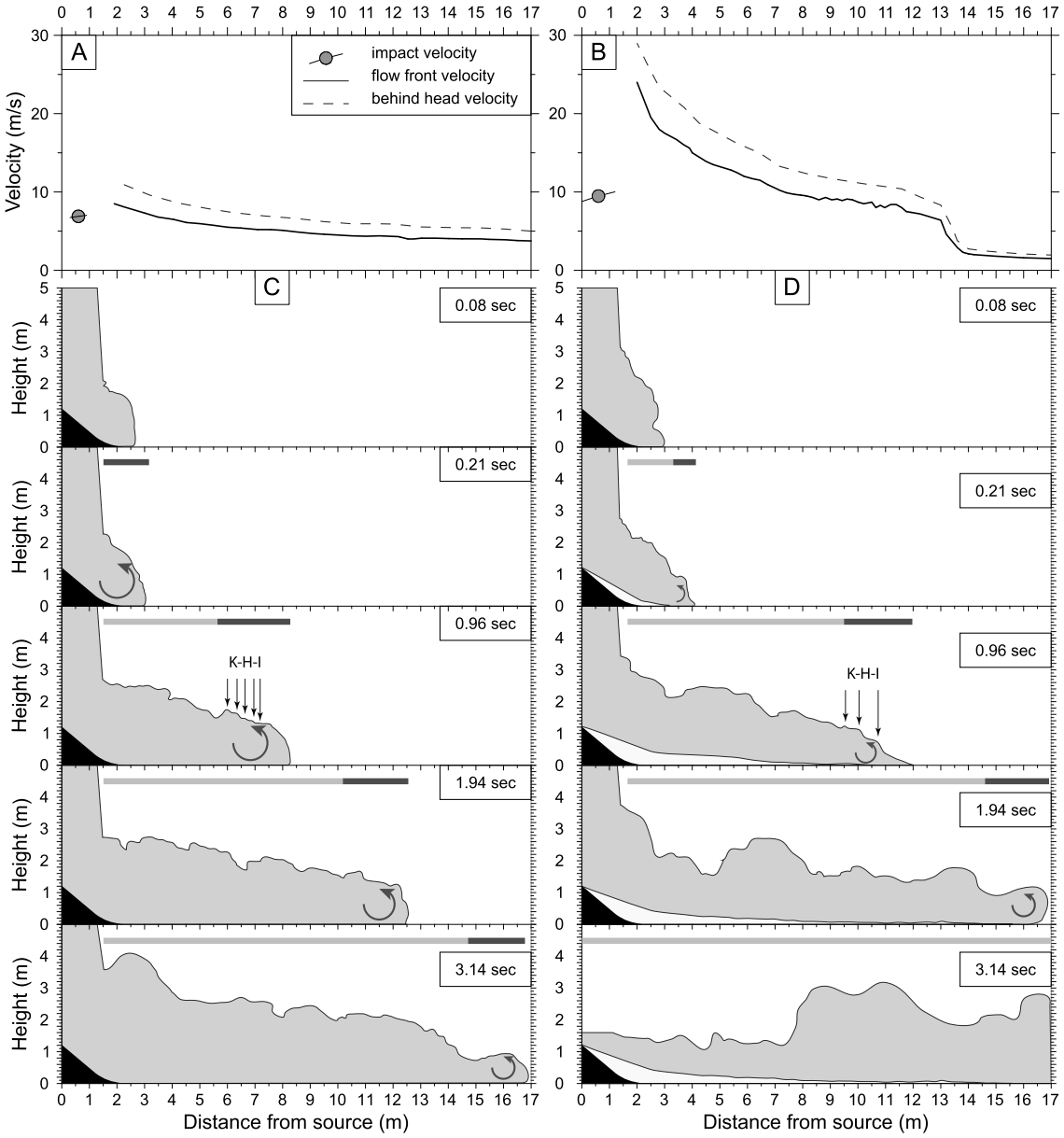

Figure 5. PDC kinematics. (a and b) Flow front and maximum internal velocities of runs S_10_8.5 and PF_10_5, respectively. (c and d) Cross-sectional flow geometry at five different times for S_10_8.5 and PF_10_5, respectively. Differently colored regions depict grey = turbulent suspension; white = dense underflow; and black = curved proximal wedge section. Thick horizontal black and grey lines demark the extents of head and body, respectively. Vertical arrows highlight Kelvin-Helmholtz instabilities on the head surface, while the leading, anticlockwise rotating head vortex is shown schematically as well.

after eruption column impact, the two experimental currents varied in particle solids concentration by an order of magnitude, while the volumes of the laterally blasting density currents differed by approximately 5.5 m^3.

3.2.3. Phase (3)

The pyroclastic density current phase of the two experimental PDCs is depicted for different times at similar flow runout lengths (Figure 4) and for similar times after column impact (Figures 5c and 5d). For comparison purposes, all times reported from hereon are those after initial column collapse impact.

3.2.3.1. Experiment S_10_8.5

Within the first 3 m, the dilute flow developed a gravity current *head* (Figure 4a at 0.342 s and Figure 5c at 0.08 and 0.21 s) as a leading, up to 2 m thick, anticlockwise rotating vortex. It comprised a lower, protruding front detached from the ground by 0.05–0.1 m (nose) showing air entrainment from below; an approximately 80–90° steep middle part from 0.15–0.95 m with the highest front velocities; and an approximately 60° steep upper part.

From approximately 0.5 s onward (Figures 4a and 4c and Figure 5c at 0.96 s), 0.1–0.2 m sized, anticlockwise rotating shear instabilities developed at the upper part of the head vortex. These Kelvin-Helmholtz billows grew in size up to approximately 0.5 m before breaking apart at the rear of the head into series of clockwise and anticlockwise rotating eddies and marking the transition between the head and *body* regions. Strong air entrainment in the upper part of the body (the wake) caused progressive flow thickening up to approximately 3 m (Figure 4a at 0.708–1.791 s). From approximately 0.4 s onward, the dilute upper part of the flow spilled over the channel walls to develop ash cloud surges that spread laterally. Beyond the break-in slope at 12 m and along the open horizontal section, strong air entrainment also occurred from the sides and the head became progressively wider and shallower (Figures 4c and 5d at 3.14 s).

Overall, the flow front steadily decelerated from 8.5 m s^{-1} at 1.9 m to 3.75 m s^{-1} at 17 m (Figure 5a). The fastest flow internal velocities (U_{l_max}) always occurred behind the flow front in the rear of the leading, anticlockwise rotating head vortex. These maximum velocities are roughly 30% higher than the front velocities. Thus, the flow front was continuously replenished with faster-flowing material from behind. After approximately 25 m, the front decelerated more rapidly to ~$>2\times10^{-1}$ m s^{-1} by 30 m from impact.

3.2.3.2. Experiment PDC PF_10_5

Flow front velocities of the dense experiment PF_10_5 steadily decreased from 24 m s^{-1} (at 2 m; U_{l_max} = 29 m s^{-1}) to 6.5 m s^{-1} (at 13 m; U_{l_max} = 8.3 m s^{-1}) (Figure 5b). The highest flow internal velocities occurred behind the flow front in between the rear of the leading, anticlockwise rotating head vortex and the leading part of the flow body. Between 13 and 14 m runout, 1 m beyond the break-in slope, a sudden drop in velocity occurs. Thereafter, front velocities gradually decrease out to 17 m before rapidly declining after 20 m.

The dense PF_10_5 current initially developed an up to 2.5 m thick front (Figure 5d at 0.08 s). By 3 m travel distance (approximately 0.1 s), an approximately 0.7 m thick head developed as the leading, anticlockwise rotating vortex with a protruding nose detaching 0.1–0.15 m from the ground (Figure 4b at 0.121 s). By 4 m travel distance (approximately 0.2 s), the outline of the initially bulbous head started to change noticeably and developed a leading and shallow wedge-shaped front and a steeper rear region (Figure 5d at 0.21 s). By 5 m travel distance, anticlockwise rotating shear instabilities developed along the upper surface of the head (e.g., Figure 5d at 0.96 s). These were wider (up to 0.7 m) than similar Kelvin-Helmholtz instabilities seen in S_10_8.5. Similar to S_10_8.5, the shear instabilities grew with time but broke apart into smaller vortexes with variable sense of rotation behind the leading head vortex (marking the head-body boundary). Between 4 and 13 m travel distance, the length of the head had increased from 0.5 m to 2.4 m (Figures 4b and 5d 0.21 and 0.96 s). This was largely attributed to the progressive lengthening of the leading shallow wedge. The front of the wedge was characterized by a protruding nose detaching 0.02–0.03 m from the ground and the development of highly unsteady lobes and clefts that broke out from the front to be overridden later (Figure 4d). After 2.2 s, while moving across the unconfined, horizontal section, lateral air entrainment into the head increases. The head widened and thickened and started to override its strongly decelerating wedge-shaped front. After approximately 3 s, the slow rising of ash clouds above the PDC deposit was only strongly developed downstream of approximately 7.5 m (Figure 5d at 3.14 s).

3.2.4. Phase (4)

Expanding clouds of dilute particle and gas billowed up and out from both experiments to >10 m. These initially grow at <1 m s^{-1}, but expansion drops to <0.01 m s^{-1} after 30 s. In the dilute run S_10_8.5, ash clouds rise in a single step from basal deposited material. In PF_10_5, however, larger (up to 5 m wide) rising ash clouds developed from coalescence of smaller vortexes.

3.2.5. Turbulent Suspensions, Shifting Sand Dunes, and Dense Underflows

3.2.5.1. S_10_8.5

Figure 6a captures the passage of the complete head region and the beginning of the body region of the current at 5.5 m. In the frontal part of the head, particles are continuously suspended. A subvertical frontal geometry indicates similar velocities between the slightly raised head base (>0.05 m) and up to about 0.9 m above this. In this rear of the head, a large anticlockwise rotating head vortex billowed across the 0.6 m high channel wall (circles in Figure 6). Above approximately 0.5 m, eddies are roughly circular (in cross-sectional view); in the basal flow, they are flattened and deformed (black arrows). Roughly 1.3 s after column impact, a diffuse boundary developed in the flow body between an upper stratified and turbulent flow and a thin, denser basal region (white dashed line). In high-speed videos it was observed that the basal region consists of 2–4 cm tick sand waves, formed by rolling and saltating particles. For the majority of the flow passage,

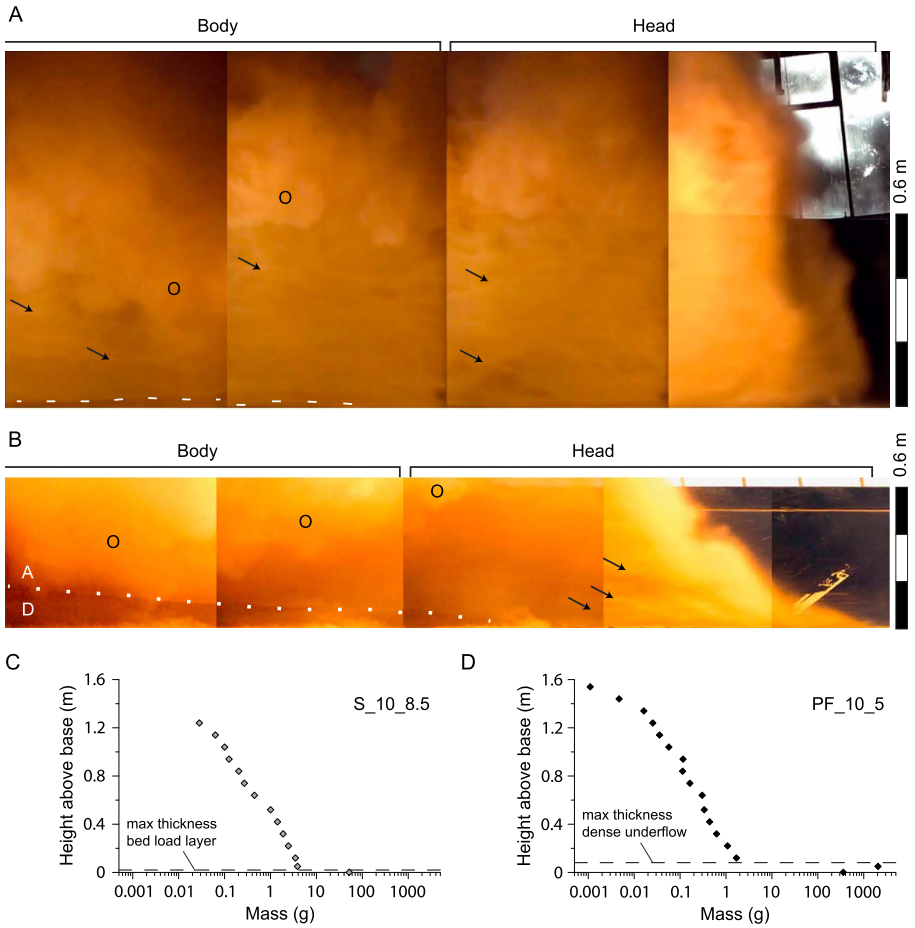

Figure 6. Longitudinal and vertical stratification of experimental PDCs. (a and b) Image cross sections of the lower 1.05 m (S_10_8.5) and 0.65 m (PF_10_5) of the PDCs obtained by stitching frames of 1.22 s (S_10_8.5) and 0.58 s long (PF_10_5) high-speed sequences, which were recorded at a runout distance of 5.5 m. Note that the horizontal scale in both images is strongly condensed toward the flow body for illustration purposes. Circles mark ash cloud spilling sideways over channel. Arrows point toward stretched eddies. (c and d) Mass collected in vertical arrays of flow samplers (4.91 cm^2 sampler cross section) at different heights for S_10_8.5 and PF_10_5, respectively. The lower two points for PF_10_5 are estimates based from time-integrated velocity point measurements using particle image velocimetry multiplied by sample area (4.91 cm^2) and material noncompacted density (900 kg m^{-3}) and divided by the flow duration (dense flow arrival to deposition). Dashed line indicates maximum thickness of basal region of saltation, rolling, and shifting sand waves for S_10_8.5 and maximum thickness of dense underflow in PF_10_5.

no deposition occurs and sand waves transit the view area. Deposition commences around 2.5–3 s after column impact, in the form of strongly stratified, generally upward fining dunes. The strongly vertical stratification is also noted in a 3 orders of magnitude drop in deposited mass over samplers placed vertically up to 1.24 m at the 8.5 m runout point (Figure 6c). Bed load deposition is confined between 0.01 and 0.15 m. Integration of the data shows that approximately 78% of the flowing mass was transported in the bed load layer.

3.2.5.2. PF_10_5

Figure 6b depicts the passage of the nose, head, and leading body regions of the experimental PDC at 5.5 m. The nose was preceded by saltating pumice lapilli ejected forward from the nose and head regions. Above an approximately 2 cm thick, saltating basal layer, particles in the nose and head regions are transported in turbulent suspension. As in S_10_8.4, homogeneous suspension and circular-shaped eddies occur in the upper proportion of the ash cloud, while stretched eddies concentrate toward the base of the flow. Approximately 1 s after column impact, a diffuse boundary between the upper ash cloud and a dense basal underflow appears (white dotted line). This interface became more defined by 1.2 s after column impact. The basal flow moves as a granular shear flow with a high basal slip velocity and with downward and upward migrating surface waves at its upper boundary toward the ash cloud. Deposition from the base upward started after

approximately 2 s. In the flow sediment samplers at 8.5 m, sample mass varied over 5 orders of magnitude in the lower 1.24 m (Figure 6d). In this case, 99.7% of the mass was transported in the dense underflow. Despite initial mass discharge rates of 14.5 times that of the dilute experiment, absolute values of mass transported at the same flow levels in turbulent suspension at the 8.5 m observation point are 50% lower than in S_10_8.5.

3.3. PELE Experimental Deposits

Run S_10_8.5 reached 35 m of runout (before being blocked by an 8 m cliff) and PF_10_5 traveled 24 m, while in both cases the very thin distal margins were redeposited by crosswinds before the ash cloud settled completely.

3.3.1. S_10_8.5

Along the channel axis, the deposit forms a clear longitudinal wedge, from proximally 6 cm (against wall; 15 cm in channel) to submillimeter thicknesses at distal margins (Figure 7a). Up to 10.5 m runout within the channel, strong thickness variations occur in dunes of poorly sorted stratified and laminated ash and lapilli. Dunes range between 1.8 m down to 0.25 m length and 0.15 m down to 0.015 m in height (Figures 7b and 7c). Beyond 10.5, dunes disappear and the deposit is composed of millimeter to submillimeter laminations of very fine ($<$63 μm) to coarse ash ($<$2 mm) and rare lapilli ($>$2 mm). Laterally, laminated, normally graded ash deposits from the expanded cloud of ash are 15 mm near the channel and thin to very fine "dust" layers at 8.25 m outward.

3.3.2. PF_10_5

This deposit formed a steep longitudinal wedge, from 0.67 m in proximal thickness to submillimeter traces of fine ash at the margins (Figure 7a). Up to 16 m, the dense underflow emplaced coarse-grained deposits that grade from proximally stratified coarse to fine ash beds, into faintly stratified or massive fine ash beds, grading up to coarse ash with a capping of isolated pumice lapilli (Figure 7e). At 16 m the underflow deposit shows an ~3.5 m wide, lobate front (Figure 7d).

From approximately 4 to 15 m, the deposit was aerated for several minutes after deposition before collapsing to form an undulating surface. Gas escape pipes and elliptical gas pockets are visible in vertical cross sections (Figure 7e). Farther downstream, deposits emplaced by the slowing wedge-shaped front of the head are $<$3 mm thick, laminated and normally graded fine ash. The millimeter-thick deposits from the dilute overriding ash cloud deposits show similar characteristics as in S_10_8.5 but are slightly thinner, forming laterally around the channel and downstream of the main body runout.

4. Final Discussion and Outlook

PELE was designed as a large-scale facility, where well-scaled PDC analogues can be repeatedly synthesized to study many aspects of their dynamics in safety. So far, $>$50 experimental runs have been conducted to explore the range of setup conditions through systematic variations of discharge height, discharge mass, discharge rate, channel inclination and width, and initial grain size distribution. These experiments delineate the typical length scale and timescales of gas-particle transport necessary to assess the scaling similitude to natural currents. Currently, on-going series of experiments will complete testing of other experimental parameters including mixture temperature and floor roughness.

The experimental runs S_10_8.5 and PF_10_5 described here illustrate the breadth of PDC transport and deposition dynamics that can be produced in the current PELE setup. S_10_8.5 with an initial particle concentration C_I of 0.6 vol % and maximum particle velocities of 9 m s^{-1} showed many characteristics analogous to natural dilute PDCs. The flow attained strong density stratification in the proximal meters and included a lower, $<$ 5 cm thick region of shifting sand waves, rolling and saltating particles, and an upper, 1.5–4.5 m thick zone where particles were transported in fully turbulent suspension. Experimental deposits ranged from dune-bedded facies and laminated beds emplaced under tractional conditions to thin dusting blankets of ash clouds. By contrast, PF_10_5 with an initial particle concentration of 7.8 vol % and maximum flow internal velocities of 29 m s^{-1} revealed conditions akin to dense PDCs or pyroclastic flows. Particle settling in the 1.5–3.8 m thick shear flow led to the formation of a dense basal underflow with an upper, overriding ash cloud. Deposits emplaced by the dense underflow show many features of natural pyroclastic flow deposits, including stratified and massive depositional units, inverse grading and coarse-rich tops, lobate fronts, aerated and fluffy deposits with degassing pipes, and entrapped gas-rich zones. Thinly laminated and fine-grained

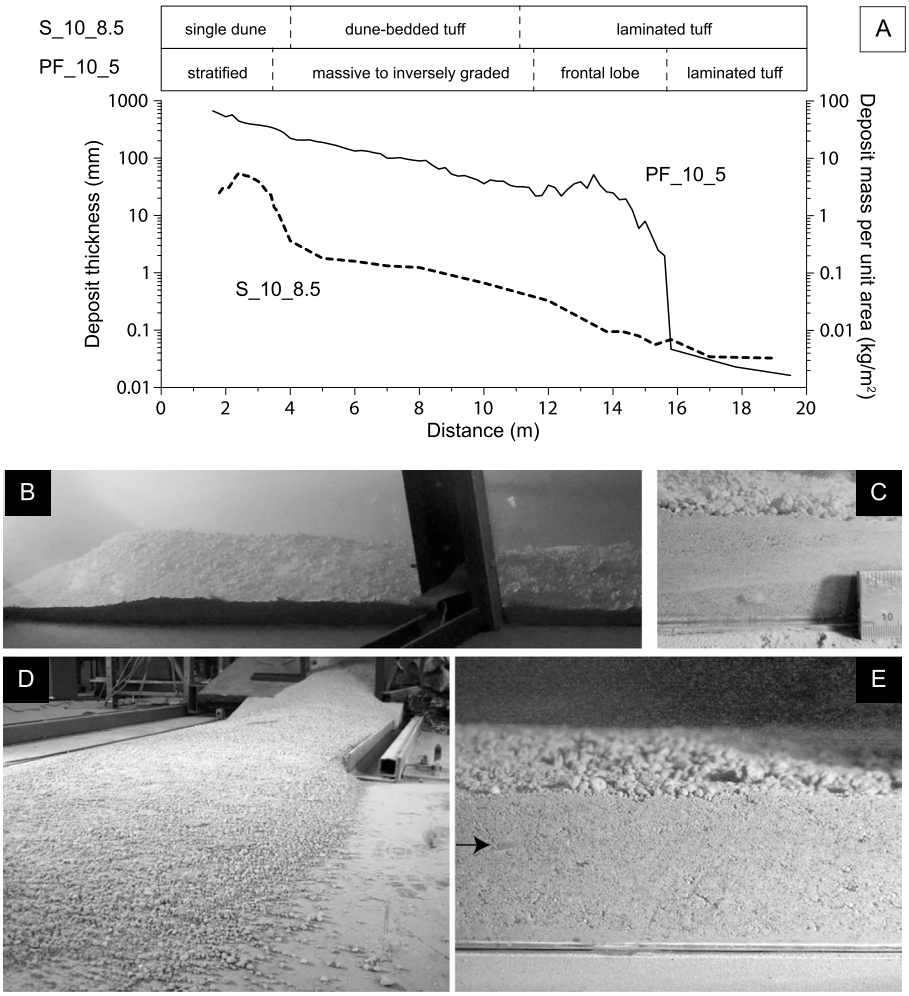

Figure 7. PDC deposits. (a) Deposit thickness and transient bed form facies for S_10_8.5 and PF_10_5. (b) Dune bed form of 1.8 m long and up to 15 cm high produced in S_10_8.5. (c) Close-up of a cross-sectional view of the dune shown in Figure 7b. (d) Frontal lobe of PF_10_5 at 15.5 m. (e) Cross-sectional view of the medial, aerated, massive deposit with a top plaster of pumice lapilli of PF_10_5. Gas pockets and gas elutriation pipes (e.g., arrow) are also seen.

facies emplaced by the leading gravity current head and by the overriding ash cloud surge show similarities to real-world ground layer and veneer deposits, respectively.

The particle concentration of dense underflows can be estimated by comparing its thickness in the medial to distal regions (where it is almost constant over a few meters) just prior to deposition onset and after deposition and final compaction. This gives values between 750 and 850 kg m^{-3} that are up to 10% lower than the noncompacted material bulk density. Thicknesses of 0.1 to 10 mm of medial to distal ash cloud surge deposits compared to flow thicknesses of 1.5 and 3.8 m yield depth-averaged particle concentrations between 10^{-1} and 10^{-4} vol %.

Several authors have highlighted that classical experimental PDCs of liquid particle gravity currents do not reach turbulence scales comparable to natural flows [*Burgisser et al.*, 2005; *Dellino et al.*, 2007; *Andrews and Manga*, 2012]. Recent laboratory experiments conducted on turbulent air-talcum powder flows investigating the dynamics of coignimbrite clouds partially overcame this problem [*Andrews and Manga*, 2011], but orders of magnitude differences in the Reynolds number, the Stokes number, and also the Stability number still pose strong limitations in comparing experimental flows and deposits to real-world PDCs. The first experiments to close the gap between analogue and natural dilute PDCs (e.g., maximum *Re* of 10^6) were those of Dellino and colleagues [e.g., *Dellino et al.*, 2007, 2010, 2014]. The pioneering large-scale gas-particle flows fed from highly unsteady column collapses also produced deposit bed forms comparable to nature.

Table 2. Bulk Flow Scaling Parameters of Natural Dilute PDCs and Experimental Currents and Comparison of Nondimensional Deposit Length Scales

Parameter	Unit	Range	Natural Dilute PDCs	PELE Bulk Flow
Particle diameter	mm	Min	0.015[a]	0.004
		Max	1024[a]	22
Dynamic viscosity	Pa s	Min	10E−05[a]	10E−05
		Max	10E−05[a]	10E−03
Fluid density	kg m^{-3}	Min	1[a]	1
		Max	1[a]	8
Particle density	kg m^{-3}	Min	1000[a]	400
		Max	2500[a]	2600
Flow velocity	m s^{-1}	Min	10[a]	<2
		Max	200[a]	30
Flow height	m	Min	10[a]	0.75
		Max	1000[a]	4
Reynolds number		Min	3.3E+06	1.5E+04
		Max	6.7E+09	2.8E+07
Stokes number		Min	1.1E−03	7.4E−05
		Max	9.7E+07	4.64E+04
Stability number		Min	2.8E−06	7.1E−07
		Max	9.7E+09	4.6E+05
Particle Froude number		Min	1E−01	3E−01
		Max	2E+01	1E+01
Richardson number		Min	2E−04	1E−03
		Max	1.1E+01	4.5E+01
Dune amplitude: flow thickness		Min	1E−05[b]	2.5E−03
		Max	3E−02[b]	1.5E−01
Deposit area: volume ^ 2/3		Min	2E+02	1E+02
		Max	2E+03	2E+03

[a]Data taken from *Burgisser et al.* [2005].
[b]Dune data from *Sigurdsson et al.* [1987].

The gas-particle PDC analogues generated in our new large-scale facility extend this overlap in dynamic and kinematic scaling parameters further. The available parameter space to vary the kinematic and boundary conditions of gas-pyroclast suspensions in controlled column collapses allows synthesizing transport and deposition modes that range from dilute pyroclastic surge-like PDCs to concentrated pyroclastic flow-like PDCs. The use of natural pyroclastic material (with their natural particle characteristics) and air ensures natural stress coupling between solid and fluid phases. Table 2 compares the ranges in nondimensional scaling factors of the experimental turbulent suspension currents (data from dilute PDC experiments like S_10_8.5 and ash cloud surges of moderate to dense experiments like PF_10_5) with data compiled for natural dilute PDCs [*Burgisser et al.*, 2005]. All experiments conducted thus far produce fully turbulent conditions with maximum Reynolds numbers well in the 10^6 range. At large discharge heights and moderate initial dilutions Reynolds number for a significant part of runout even reached values at the lower end of 10^7. Large overlaps in scaling parameters for the Richardson, Froude, Stokes, and Stability numbers further constrain the scaling similitude at small, large, and intermediate scales of turbulence (Table 2 and Figures 8a and 8b). Table 3 also shows that granular scaling parameters characterizing the dense underflows generated in experiments with moderate to dense initial particle concentrations C_I match those approximated for natural pyroclastic flows.

No large-scale experiment yet conducted produces complete overlap in all natural scales. The natural range in PDC transport and deposition regimes already varies so greatly that the dynamics of small-volume, granular-type PDCs are fundamentally different from those in large-volume ignimbrites and phreatomagmatic surges. We also suspect that certain aspects of large-volume PDC runout and sedimentation require length scale and timescales of gas-particle interaction that do not occur in small-medium volume PDCs and large-scale experiments. One preliminary objective for the construction of the large-scale facility was to reproduce a large range of PDC transport conditions in specific control windows along the flow runout zone. However, the ability to vary the flow (and consequently deposition) timescales from short pulses of experimental flows

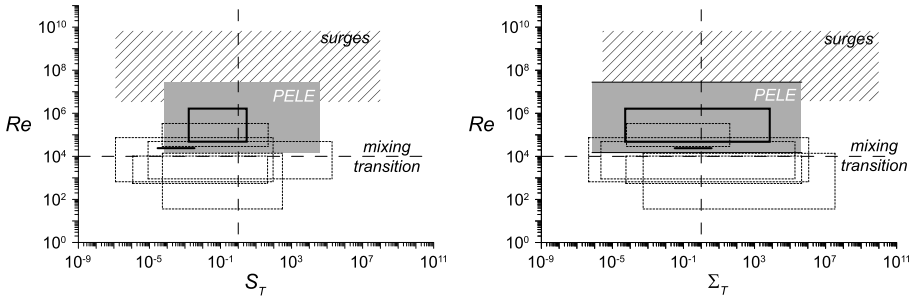

Figure 8. Estimates of Reynolds number *Re*, Stokes number S_T, and Stability number Σ_T for natural pyroclastic surges (black solid line) and the large-scale experiments (grey box). Estimates for *Re*, S_T, and $\gamma\Sigma_T$ of previous PDC analogues including particle liquid gravity currents (grey dashed lines) in water tanks [*Bonnecaze et al.*, 1995; *Choux and Druitt*, 2002; *Ghosh et al.*, 1981; *Jobson and Sayre*, 1970; *Stix*, 2001; *Woods et al.*, 1998] taken from *Burgisser et al.* [2005]. Large-scale surge experiments (back solid squares) using volcanic material and air [*Dellino et al.*, 2008, 2010, 2014] and air-talcum gravity current experiments (black solid lines) in wall-bounded channels [*Andrews and Manga*, 2011, 2012] are shown for comparison.

to sustained currents; the large range of natural deposit facies and their lateral transitions (including massive, graded, dune-bedded, stratified, and laminated bed forms); and the emplacement of bed forms large enough to record their formation in high-speed video indicates that major aspects of PDC downstream evolution can be replicated in future experiments. The strong overlap in geometric scaling parameters of natural and experimental deposits, including the mobility ratio $A/V^{2/3}$ (A being the deposit footprint and V the deposit volume) or the nondimensional dune heights (Table 2), supports this view.

Table 3. Scaling Parameters of Natural Concentrated PDCs (Natural PFs) and for the Dense Underflow in the Large-Scale Experiments

Parameter	Unit	Range	Natural PFs	PELE Dense Underflow
Median particle diameter	mm	Min	2E−02[a]	2.6E−01
		Max	5E−01[a]	3.7E−01
Particle bulk density	kg m^{-3}	Min	500[a]	850
		Max	2500[a]	2000
Particle volume fraction		Min	0.3[a]	0.2
		Max	0.6[a]	0.6
Flow thickness	m	Min	1[a]	0.1
		Max	50[a]	0.6
Flow length	m	Min	1E+03[a]	15
		Max	1E+04[a]	25
Velocity	m s^{-1}	Min	5[a]	1.5
		Max	30[a]	15
Hydraulic permeability	m^2	Min	1E−12[a]	1E−11
		Max	1E−10[a]	4E−11
Slope	deg	Min	0.1[a]	5
		Max	30[a]	25
Mass number		Min	1E+02	1E+02
		Max	2E+03	1.5E+03
Froude number		Min	1.6	1.5
		Max	9.6	6.2
Bagnold number		Min	1E−02	1E+00
		Max	1E+02	1E+02
Darcy number		Min	1E+02	1E+00
		Max	1E+04	1E+03
Fluidization number		Min	1E−07	1E−05
		Max	1E−03	1E−03
Pore pressure number		Min	1E−04	1E−02
		Max	1E+01	1E+02
Savage number		Min	1E−09	1E−06
		Max	1E−07	1E−05

[a]Data taken from *Roche* [2012], which is based on *Iverson and Denlinger* [2001].

Future large-scale experiments will focus on quantifying the dynamics inside moving PDCs to characterize their transport, runout, and deposition processes. Systematic variations in particle grain size distribution, initial kinematic conditions of column collapse, channel geometry, and flow temperature will provide the necessary fundamental measurements to test and further develop current physical concepts of these hazardous phenomena.

Acknowledgments

PELE was constructed with the financial support of the Royal Society of New Zealand Marsden Fund to S.C., G.L., and J.J. (MAU0906) also providing a PhD scholarship for E.B. We would also like to acknowledge the generous financial support by Massey University and by the Living with Volcanic Risk Programme within the New Zealand Natural Hazard Research Platform (C05X0907). We thank R. Sulpizio and T. Eposti-Ongaro for their thoughtful reviews. This task would have been impossible without the enthusiastic help of many students and staff at Massey University including Kate Arentsen, Clive Bardell, Daniel Farley, David Feek, Olaf Griewaldt, Matt Irwin, Damian Jones, Gabor Kereszturi, Anja Moebis, Adam Neather, Rickus Van Niekerk, Richard Saunders, Ian Thomas, Bob Toes, Rafael Torres, Manuela Tost, Frederieke Von Schlippe, Anthony Wade, David Wiltshire, and the engineers of Streamline Engineering, especially Mervin Jones. G.L. (g.lube@massey.ac.nz) curates the data presented in this article.

References

Andrews, B. J., and M. Manga (2011), Effect of topography on pyroclastic density current runout and formation of coignimbrites, *Geology*, *39*, 1099–1102.

Andrews, B. J., and M. Manga (2012), Experimental study of turbulence, sedimentation, and coignimbrite mass partitioning in dilute pyroclastic density currents, *J. Volcanol. Geotherm. Res.*, *225–226*, 30–44.

Bonnecaze, R. T., M. A. Hallworth, H. E. Huppert, and J. R. Lister (1995), Axisymmetric particle-driven gravity currents, *J. Fluid Mech.*, *294*, 93–121.

Burgisser, A., G. W. Bergantz, and R. E. Breidenthal (2005), Addressing complexity in laboratory experiments: The scaling of dilute multiphase flows in magmatic system, *Bull. Volcanol.*, *241*, 245–265.

Calder, E. S., P. D. Cole, W. D. Dade, T. H. Druitt, R. P. Hoblitt, H. E. Huppert, L. Ritchie, R. S. J. Sparks, and S. R. Young (1999), Mobility of pyroclastic flows and surges at the Soufriere Hills volcano, Montserrat, *Geophys. Res. Lett.*, *26*, 537–540, doi:10.1029/1999GL900051.

Choux, C. M., and T. H. Druitt (2002), Analogue study of particle segregation in pyroclastic density currents, with implications for the emplacements mechanisms of large ignimbrites, *Sedimentology*, *49*, 907–928.

Cronin, S. J., G. Lube, D. S. Dayudi, S. Sumarti, S. Subrandiyo, and Surono (2013), Insights into the October–November 2010 Gunung Merapi eruption (Central Java, Indonesia) from the stratigraphy, volume and characteristics of its pyroclastic deposits, *J. Volcanol. Geotherm. Res.*, *261*, 244–259.

Dellino, P., B. Zimanowski, R. Büttner, L. La Volpe, D. Mele, and R. Sulpizio (2007), Large-scale experiments on the mechanics of pyroclastic flows: Design, engineering, and first results, *J. Geophys. Res.*, *112*, B04202, doi:10.1029/2006JB004313.

Dellino, P., R. Mele, R. Sulpizio, L. La Volpe, and G. Braia (2008), A method for the calculation of the impact parameters of dilute pyroclastic density currents based on deposit particle characteristics, *J. Geophys. Res.*, *113*, B07206, doi:10.1029/2007JB005365.

Dellino, P., et al. (2010), Conduit flow experiments help constraining the regime of explosive eruptions, *J. Geophys. Res.*, *115*, B04204, doi:10.1029/2009JB006781.

Dellino, P., et al. (2014), Volcanic jets, plumes, and collapsing fountains: Evidence from large-scale experiments, with particular emphasis on the entrainment rate, *Bull. Volcanol.*, *76*, 834.

Freundt, A., and M. I. Bursik (1998), Pyroclastic flow transport mechanisms, in *From Magma to Tephra: Modelling Physical Processes of Explosive Volcanic Eruptions, Dev. Volcanol.*, vol. 4, edited by A. Freundt and M. Rosi, pp. 173–245, Elsevier, Amsterdam, Netherlands.

Freundt, A., C. J. N. Wilson, and S. N. Carey (2000), Ignimbrites and block-and-ash flows deposits, in *Encyclopedia of Volcanoes*, edited by H. Sigurdsson et al., pp. 581–600, Academic Press, London.

Ghosh, J. K., B. S. Mazumdmer, and S. Sengupta (1981), Methods of computation of suspended load from bed materials and flow parameters, *Sedimentology*, *28*, 781–791.

Hoblitt, R. P., C. D. Miller, and J. W. Vallance (1981), Origin and stratigraphy of the deposit produced by the May 18 directed blast, in *The 1980 Eruptions of Mount St. Helens, Washington*, edited by P. W. Lipman and D. R. Mullineaux, *U.S. Geol. Surv. Prof. Pap.*, *1250*, 401–419.

Iverson, R. M., and R. P. Denlinger (2001), Flow of variably fluidized granular masses across three-dimensional terrain: 1. Coulomb mixture theory, *J. Geophys. Res.*, *106*, 537–552, doi:10.1029/2000JB900329.

Jenkins, S., J.-C. Komorowski, P. J. Baxter, R. Spence, A. Picquout, F. Lavigne, and Surono (2013), The Merapi 2010 eruption: An interdisciplinary assessment methodology for studying pyroclastic density currents, *J. Volcanol. Geotherm. Res.*, *261*, 316–329.

Jobson, H. E., and W. W. Sayre (1970), Vertical transfer in open channel flow, *J. Hydraul. Div., Proc. Am. Soc. Civ. Eng.*, *96*, 703–724.

Levine, A., and S. Kieffer (1991), Hydraulics of the August 7, 1980, pyroclastic flow at Mount St. Helens, Washington, *Geology*, *19*, 1121–1124.

Lube, G., S. J. Cronin, J.-C. Thouret, and Surono (2011), Kinematic characteristics of pyroclastic density currents at Merapi and controls of their avulsion from natural and engineered channels, *Geol. Soc. Am. Bull.*, *123*, 1127–1140.

Roche, O. (2012), Depositional processes and gas pore pressure in pyroclastic flows: An experimental perspective, *Bull. Volcanol.*, *74*, 1807–1820.

Sigurdsson, H., S. N. Carey, and R. V. Fisher (1987), The 1982 eruption of El Chichon Volcano, Mexico: 3. Physical properties of pyroclastic surges, *Bull. Volcanol.*, *49*, 467–488.

Stix, J. (2001), Flow evolution of experimental gravity currents: Implications for pyroclastic flows at volcanoes, *J. Geol.*, *109*, 381–398.

Sulpizio, R., P. Dellino, D. M. Doronzo, and D. Sarocchi (2014), Pyroclastic density currents: State of the art and perspectives, *J. Volcanol. Geotherm. Res.*, *283*, 36–65.

Taylor, G. A. (1958), The 1951 eruption of Mount Lamington, Papua: Australia Bureau of Mineral Resources, *Geol. Geophys. Bull.*, *38*, 117.

Thielicke, W., and E. J. Stamhuis (2014), PIVlab—Towards user-friendly, affordable and accurate digital particle image velocimetry in MATLAB, *J. Open Res. Software*, *2*(1), e30, doi:10.5334/jors.bl.

Valentine, G. A. (1998), Damage to structures by pyroclastic flows and surges, inferred from nuclear weapons effects, *J. Volcanol. Geotherm. Res.*, *87*, 117–140.

Valentine, G. A., C. Bonadonna, I. Manzella, A. Clarke, and P. Dellino (2011), Large-scale experiments on volcanic processes, *Eos Trans. AGU*, *92*, 89–96, doi:10.1029/2011EO110001.

Waitt, R. B. J. (1981), Devastating pyroclastic density flow and attendant air fall of May 18—Stratigraphy and sedimentology of deposits, in *The 1980 Eruptions of Mount St. Helens, Washington*, edited by P. W. Lipman and D. R. Mullineaux, *U.S. Geol. Surv. Prof. Pap.*, *1250*, 439–458.

Wilson, C. J. N. (1985), The Taupo eruption, New Zealand II. The Taupo Ignimbrite, *Philos. Trans. R. Soc. London, Ser. A*, *314*(1529), 229–310.

Wohletz, K. H. (1998), Pyroclastic surges and compressible two-phase flow, in *From Magma to Tephra*, edited by A. Freundt and M. Rosi, pp. 247–312, Elsevier, Amsterdam, Netherlands.

Woods, A. W., M. I. Bursik, and A. V. Kurbatov (1998), The interaction of ash flows with ridges, *Bull. Volcanol.*, *60*, 38–51.